Accepted Manuscript

Energy balance and mass conservation in reduced order models of fluid flows

Muhammad Mohebujjaman, Leo G. Rebholz, Xuping Xie, Traian Iliescu
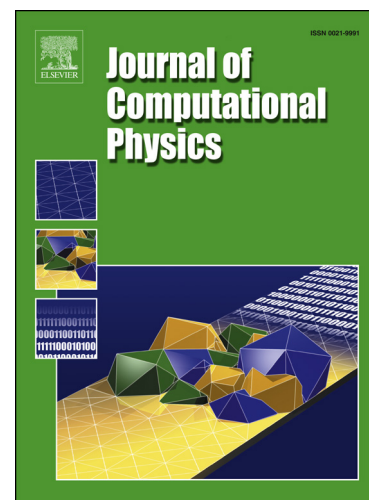
Please cite this article in press as: M. Mohebujjaman et al., Energy balance and mass conservation in reduced order models of fluid flows, *J. Comput. Phys.* (2017), http://dx.doi.org/10.1016/j.jcp.2017.06.019

Energy Balance and Mass Conservation
in Reduced Order Models of Fluid Flows

Muhammad Mohebujjaman[a], Leo G. Rebholz[a,*], Xuping Xie[b], Traian Iliescu[b],

[a]*Department of Mathematical Sciences, Clemson University, Clemson, SC 29634, U.S.A.*
[b]*Department of Mathematics, Virginia Tech, Blacksburg, VA 24061, U.S.A.*

Abstract

In this paper, we investigate theoretically and computationally the conservation properties of reduced order models (ROMs) for fluid flows. Specifically, we investigate whether the ROMs satisfy the same (or similar) energy balance and mass conservation as those satisfied by the Navier-Stokes equations. All of our theoretical findings are illustrated and tested in numerical simulations of a 2D flow past a circular cylinder at a Reynolds number $Re = 100$.

First, we investigate the ROM energy balance. We show that using the snapshot average for the centering trajectory (which is a popular treatment of nonhomogeneous boundary conditions in ROMs) yields an incorrect energy balance. Then, we propose a new approach, in which we replace the snapshot average with the Stokes extension. Theoretically, the Stokes extension produces an accurate energy balance. Numerically, the Stokes extension yields more accurate results than the standard snapshot average, especially for longer time intervals.

Our second contribution centers around ROM mass conservation. We consider ROMs created using two types of finite elements: the standard Taylor-Hood (TH) element, which satisfies the mass conservation weakly, and the Scott-Vogelius (SV) element, which satisfies the mass conservation pointwise. Theoretically, the error estimates for the SV-ROM are sharper than those for the TH-ROM. Numerically, the SV-ROM yields significantly more accurate results, especially for coarser meshes and longer time intervals.

Keywords: Reduced order model, proper orthogonal decomposition, energy balance, mass conservation.

1. Introduction

Reduced order models (ROMs) have been used in numerous scientific and engineering applications, and have been particularly successful as surrogate models for structure dominated fluid flows (see e.g. the nice review of Lassila et al in [1] and references therein). The ROM strategy is straightforward: In an offline stage, snapshots from a fine resolution numerical simulation of the

---

*corresponding author

Email addresses: `mmohebu@clemson.edu` (Muhammad Mohebujjaman), `rebholz@clemson.edu` (Leo G. Rebholz), `xupingxy@vt.edu` (Xuping Xie), `iliescu@vt.edu` (Traian Iliescu)

URL: `https://mthsc.clemson.edu/directory/viewperson.py?personid=358` (Muhammad Mohebujjaman), `http://www.math.clemson.edu/~rebholz` (Leo G. Rebholz), `http://www.math.vt.edu/people/xupingxy` (Xuping Xie), `http://www.math.vt.edu/people/iliescu` (Traian Iliescu)

underlying system are used to create a ROM basis, which is then used within a Galerkin framework to create the ROM. In an online stage, this ROM is used as a surrogate model in a predictive regime, i.e., either on a time interval longer than that in which the snapshots were generated, or at parameters different from those used in the snapshot generation.

In this paper, we consider the *conservation properties* of ROMs used as a surrogate model of the incompressible Navier-Stokes equations, i.e., whether the ROM satisfies the same (or similar) conservation laws as those satisfied by the corresponding continuous system. Better adherence of discrete solutions to the underlying physics, and to conservation laws in particular, generally leads to improved accuracy and stability, especially over long time intervals [2, 3, 4, 5, 6, 7, 8]. Conservation properties of ROMs have been studied in, e.g., [9, 10, 11, 12, 13, 14, 15, 16, 17, 18, 19]. Most of these studies, however, have focused on Hamiltonian systems; dissipative systems have been relatively less investigated. In this paper, we investigate the energy balance and mass conservation of standard ROMs for fluid flows governed by the incompressible Navier-Stokes equations, and to our knowledge this is the first in depth study of ROMs for fluid flow from this perspective.

Our first contribution concerns the ROM *energy balance*. We show that using the snapshot average for the centering trajectory (which is commonly used to avoid the challenging treatment of nonhomogeneous boundary conditions in ROMs) yields an energy balance that is seemingly not consistent with the energy balance of a continuous solution. Our claim is supported by numerical results for a 2D flow past a circular cylinder at a Reynolds number $Re = 100$. To 'fix' the energy balance, we propose a new approach in which we replace the standard snapshot average with the Stokes extension of the boundary condition. We show that the Stokes extension allows for the correct treatment of nonhomogeneous boundary conditions, and yields an accurate energy balance at the same time. The theoretical energy balance improvement of the Stokes extension is confirmed by numerical results, and in particular we see a significant improvement compared to the snapshot average results, especially over longer time intervals.

Our second contribution regarding the ROM conservation properties centers around ROM *mass conservation*. Specifically, we show that generating the snapshots with finite elements (FEs) that satisfy pointwise mass conservation yields significantly more accurate numerical results than those obtained with FEs that satisfy only weak mass conservation. To this end, we consider two FEs: (i) the standard *Taylor-Hood (TH)* element, which satisfies the mass conservation weakly; and (ii) the *Scott-Vogelius (SV)* element, which satisfies the mass conservation pointwise. The numerical results for the SV-ROM are significantly more accurate than those for the TH-ROM, especially for *coarser meshes* and *over long time intervals*. In addition to numerical evidence, we also give theoretical support for increased numerical accuracy of SV-ROM solution by proving error estimates, which are sharper than those for the TH-ROM.

This paper is organized as follows: In section 2, we collect some preliminaries and notation that will be used throughout the paper. In section 3, we consider the energy balance of standard ROMs when the snapshot average or the Stokes extension are used to tackle nonhomogeneous boundary conditions. In section 4, we prove error estimates for both the SV-ROM and TH-ROM and show that the former yields sharper bounds than the latter. In section 5, we illustrate the theoretical developments in sections 3–4 in the numerical simulation of a 2D flow past a circular cylinder at Reynolds number $Re = 100$. In section 6, we present conclusions and outline future research directions. Finally, in the appendix, we prove Theorem 4.1.

2

2. Notation and Preliminaries

In this section, we introduce some notation and preliminaries that will be used in what follows. We consider a domain $\Omega \subset \mathbb{R}^d$, $d = 2$ or 3, to be a connected set with Lipschitz continuous boundary. We denote the usual $L^2(\Omega)$ norm and inner product with $\|\cdot\|$ and $(\cdot, \cdot)$, respectively. Any other norms and inner products will be labeled. We will use a generic constant C in our analysis, which can change at each occurrence, and can depend on the problem data and true solution, but will be independent of the discretization parameters.

Define the skew-symmetric trilinear form b^*: $H^1(\Omega) \times H^1(\Omega) \times H^1(\Omega) \longrightarrow \mathbb{R}$ as

$$b^*(u, v, w) := \frac{1}{2}(u \cdot \nabla v, w) - \frac{1}{2}(u \cdot \nabla w, v). \tag{2.1}$$

Note that, by construction, $b^*(u, v, v) = 0$.

2.1. Navier-Stokes Equations Preliminaries

We consider herein the incompressible *Navier-Stokes equations (NSE)* with nonhomogeneous Dirichlet boundary conditions:

$$
\begin{aligned}
u_t + u \cdot \nabla u + \nabla p - \nu \Delta u &= f, \ \Omega \times (0, T], &\tag{2.2} \\
\nabla \cdot u &= 0, \ \Omega \times (0, T], &\tag{2.3} \\
u &= g(x), \ \partial\Omega \times (0, T], &\tag{2.4} \\
u(x, 0) &= u_0(x), \ \Omega. &\tag{2.5}
\end{aligned}
$$

In the case of $g = 0$, there are several subtle details regarding physical fidelity of discrete solutions that can generally be neglected. However, for $g \neq 0$, we will show that there are important considerations in ROM algorithms that can lead to more accurate discrete physics and better overall accuracy. We will assume that strong (and thus unique) solutions exist to (2.2)-(2.5).

2.2. Finite Element Preliminaries

We assume $\tau_h(\Omega)$ is a regular, conforming triangulation/tetrahedralization of Ω. We denote by $P_m(\tau_h)$ the set of degree m piecewise polynomials defined on the mesh τ_h, and define the finite element spaces by

$$
\begin{aligned}
X_h &= \{v_h \in H^1(\Omega) \cap P_m(\tau_h), \ v_h|_{\partial\Omega} = 0\}, \\
X_h^g &= \{v_h \in H^1(\Omega) \cap P_m(\tau_h), \ v_h|_{\partial\Omega} = I_h(g)\}, \\
Q_h &= \{q_h \in L_0^2(\Omega) \cap P_{m-1}(\tau_h)\},
\end{aligned}
$$

where $I_h(g)$ is an appropriate interpolation operator that will preserve discrete mass flux [20]. We assume that (X_h, Q_h) satisfies the LBB condition. In particular, we consider the (P_m, P_{m-1}) Taylor-Hood (TH) elements and (P_m, P_{m-1}^{disc}) Scott-Vogelius (SV) elements. TH elements are known to be LBB-stable on regular, conforming meshes [21]. We construct the meshes as barycenter refinements of a Delaunay meshes, so that SV elements are also LBB-stable [22, 23].

We define the discrete divergence-free velocity spaces as

$$
\begin{aligned}
V_h &= \{v_h \in X_h, \ (\nabla \cdot v_h, q_h) = 0 \ \forall q_h \in Q_h\}, \\
V_h^g &= \{v_h \in X_h^g, \ (\nabla \cdot v_h, q_h) = 0 \ \forall q_h \in Q_h\}.
\end{aligned}
$$

3

74 Note that for SV elements, since $\nabla \cdot X_h \subset Q_h$, these spaces can also be written as $V_h = \{v_h \in$
75 $X_h, \, \|\nabla \cdot v_h\| = 0\}$, $V_h^g = \{v_h \in X_h^g, \|\nabla \cdot v_h\| = 0\}$.

76   To compute the snapshots, we utilize the commonly used BDF2 temporal discretization, to-
77 gether with a FE spatial discretization with the TH and SV elements. For any positive integer M,
78 consider the time instances $t_n = n \, \Delta t$, $n = 0, \ldots, M$, where $\Delta t = T/M$. Denote the FE solution of
79 the NSE at time t_n to be u_h^n and the force at t_n to be $f^n = f(t_n)$. Set $u_h^1 \in V_h^g$ and $u_h^0 \in V_h^g$ to be
80 appropriate interpolants or projections of the initial conditions u^1 and u^0 in V_h. For $n = 1, 2, \ldots,$
81 find $(u_h^{n+1}, p_h^{n+1}) \in (X_h^g, Q_h)$ satisfying for every $(v_h, q_h) \in (X_h, Q_h)$,

$$\left(\frac{3u_h^{n+1} - 4u_h^n + u_h^{n-1}}{2\Delta t}, v_h \right) + b^* \left(u_h^{n+1}, u_h^{n+1}, v_h \right) - (p_h^{n+1}, \nabla \cdot v_h) + \nu(\nabla u_h^{n+1}, \nabla v_h) = \left(f^{n+1}, v_h \right),$$

$$(\nabla \cdot u_h, q_h) = 0,$$

82   Thanks to the LBB property holding, we can equivalently write our numerical scheme in its
83 V_h-formulation: for $n = 1, 2, \ldots,$ find $u_h^{n+1} \in V_h^g$ satisfying for every $v_h \in V_h$,

$$\left(\frac{3u_h^{n+1} - 4u_h^n + u_h^{n-1}}{2\Delta t}, v_h \right) + b^* \left(u_h^{n+1}, u_h^{n+1}, v_h \right) + \nu(\nabla u_h^{n+1}, \nabla v_h) = \left(f^{n+1}, v_h \right). \quad (2.6)$$

84   The following error estimate can be proven for solutions of (2.6), assuming a sufficiently regular
85 NSE solution [24, 25], a sufficiently small Δt, and either TH or SV elements are used:

$$\|u(t^M) - u_h^M\|^2 + \nu \, \Delta t \sum_{n=1}^{M} \|\nabla(u(t^n) - u_h^n)\|^2 \leq C \left(h^{2m} + \Delta t^4 + \left\{ \begin{array}{cc} \nu^{-1} \|p\|_{\infty,m}^2 \, h^{2m} & \text{if TH} \\ 0 & \text{if SV} \end{array} \right. \right), (2.7)$$

86 where C is independent of p, h, and Δt. Observe that the SV element solution is independent of
87 the pressure, whereas the TH solution is not robust with respect to the true solution pressure size
88 and complexity.

89 *2.3. Reduced Order Modeling Preliminaries*

90   In this section, we briefly describe the *proper orthogonal decomposition (POD)* and the standard
91 Galerkin ROM [26, 27].

92   For the snapshots $\{u_h^1, \ldots, u_h^M\}$, which in this paper are the FE solutions of (2.6) at M different
93 time instances, the POD seeks a low-dimensional basis that approximates the snapshots optimally
94 with respect to a certain norm. In this paper, we choose the commonly used L^2 norm. The solution
95 of the minimization problem is equivalent to the solution of the eigenvalue problem $YY^T M_h \varphi_j =$
96 $\lambda_j \varphi_j$, $j = 1, \ldots, N_h$, where φ_j and λ_j denote the vector of the FE coefficients of the POD basis
97 functions and the POD eigenvalues, respectively, Y denotes the snapshot matrix, whose columns
98 correspond to the FE coefficients of the snapshots, M_h denotes the FE mass matrix, and N_h is the
99 dimension of the FE space X_h. The eigenvalues are real and non-negative, so they can be ordered
100 as follows: $\lambda_1 \geq \lambda_2 \geq \ldots \geq \lambda_d \geq \lambda_{d+1} = \ldots = \lambda_{N_h} = 0$, where d is the rank of the snapshot matrix.
101 The ROM basis consists of the normalized functions $\{\varphi_j\}_{j=1}^r$, which correspond to the first $r \leq N_h$
102 largest eigenvalues. Thus, the ROM space is defined as $X_r := \text{span}\{\varphi_1, \ldots, \varphi_r\}$ and we note that
103 $X_r \subset V_h$.

4

104   The ROM approximation of the velocity is defined as

$$u_r(x,t) \equiv \sum_{j=1}^{r} a_j(t)\varphi_j(x) \,, \tag{2.8}$$

105   where $\{a_j(t)\}_{j=1}^{r}$ are the sought time-varying coefficients, which are determined by solving the
106   *Galerkin ROM (G-ROM)*: $\forall\, i = 1, \ldots, r$,

$$(u_{r,t}, \varphi_i) + \nu\,(\nabla u_r, \nabla \varphi_i) + b^*\,(u_r, u_r, \varphi_i) = \left(f^{n+1}, \varphi_i\right)\,. \tag{2.9}$$

107   In (2.10), we assumed that the modes $\{\varphi_1, \ldots, \varphi_r\}$ are perpendicular to the discrete pressure space,
108   which is the case if standard, conforming LBB stable elements (such as the TH and SV elements
109   considered in this paper) are used for the snapshot creation.

110   For the full discretization of the G-ROM (2.10), we consider the BDF2 discretization (which
111   was also used to generate the snapshots in (2.6)): Set $u_r^1 = u_r^0 = 0$. For $n = 2, 3, \ldots$, find $u_r^{n+1} \in X_r$
112   satisfying for every $\varphi_r \in X_r$,

$$\left(\frac{3u_r^{n+1} - 4u_r^n + u_r^{n-1}}{2\Delta t}, \varphi_r\right) + b^*(u_r^{n+1}, u_r^{n+1}, \varphi_r) + \nu(\nabla u_r^{n+1}, \nabla \varphi_r) = (f^{n+1}, \varphi_r)\,. \tag{2.10}$$

113   However, our analysis can be extended to most common time stepping schemes.

3. Energy Balance in ROMs

115   In this section, we consider ROMs for the unforced NSE with nonhomogeneous Dirichlet bound-
116   ary conditions (i.e., (2.2)–(2.5) with $f = 0$), and investigate whether the standard G-ROM satisfies
117   the same energy balance as the continuous NSE. To ensure that the snapshots (and the resulting
118   ROM basis functions) vanish on the boundary, we use the standard approach and write the ROM
119   velocity u_r as $u_r = U_h + w_r$, where $U_h = g$ on the boundary and w_r are the ROM fluctuations. For
120   U_h, we consider two cases: (i) the Stokes extension (which, to our knowledge, is new in the ROM
121   setting), and (ii) the average of the snapshots (which is the most popular approach [26, 27]). We
122   will show that in case (i) the standard G-ROM satisfies the same energy balance as the continuous
123   level NSE. For case (ii), however, there does not appear to be a continuous level energy balance
124   that matches the discrete balance dictated by this choice of U_h; we expand on this below.

3.1. Energy Balance for U_h as the Stokes Extension

126   We first derive a continuous level energy balance for the NSE, and then we show the associated
127   ROM has the same energy balance. Define U to be the (continuous level) Stokes extension of the
128   time-independent boundary condition g into Ω:

$$\begin{aligned} \nabla\lambda - \Delta U &= 0, \\ \nabla \cdot U &= 0, \\ U|_{\partial\Omega} &= g. \end{aligned}$$

129   Assuming a sufficiently regular and unique NSE solution, we can derive a continuous energy balance.
130   Write $u = U + w$, and decompose the momentum equation as

$$w_t + U \cdot \nabla w + w \cdot \nabla U + w \cdot \nabla w + \nabla p - \nu\Delta U - \nu\Delta w = -U \cdot \nabla U.$$

5

131 Using the definition of U above, we can write $\tilde{p} = p - \nu\lambda$ and obtain the equation

$$w_t + U \cdot \nabla w + w \cdot \nabla U + w \cdot \nabla w + \nabla\tilde{p} - \nu\Delta w = -U \cdot \nabla U.$$

132 Noting that w has homogenous Dirichlet boundary conditions and is also divergence-free (by con-
133 struction), we test this equation with w to vanish the first and third nonlinear terms as well as the
134 pressure term to obtain

$$\int_\Omega \frac{1}{2}\frac{d}{dt}|w|^2 \; dx + (w \cdot \nabla U, w) + \nu\|\nabla w\|^2 = -(U \cdot \nabla U, w).$$

135 Combining the nonlinear terms provides an exact balance for the energy of the fluctuations, which
136 we regard as an energy conservation law in this setting:

$$\frac{d}{dt}\frac{1}{2}\|w(t)\|^2 + \nu\|\nabla w\|^2 = -(u \cdot \nabla U, w). \tag{3.1}$$

137 This also provides an exact balance for a modified energy definition $\tilde{E}(t) = \frac{1}{2}\left(\|w(t)\|^2 + \|U\|^2\right)$:

$$\frac{d}{dt}\tilde{E}(t) + \nu\|\nabla w\|^2 = -(u \cdot \nabla U, w). \tag{3.2}$$

138   Consider now the discrete case, with U_h analogously defined to be the discrete Stokes extension
139 of the boundary condition: Find $(U_h, \lambda_h) \in (X_h^g, Q_h)$ satisfying

$$
\begin{aligned}
-(\lambda_h, \nabla \cdot v_h) + (\nabla U_h, \nabla v_h) &= 0 \; \forall v_h \in X_h, \tag{3.3}\\
(\nabla \cdot U_h, Q_h) &= 0 \; \forall q_h \in Q_h. \tag{3.4}
\end{aligned}
$$

140 Note due to LBB, this is equivalent to: Find $U_h \in V_h^g$ satisfying

$$(\nabla U_h, \nabla v_h) = 0 \; \forall v_h \in V_h. \tag{3.5}$$

141 Assuming the snapshots are created in LBB-stable spaces (X_h, Q_h), the ROM takes the form
142 (suppressing a temporal discretization): Find $w_r(t) \in X_r \subset V_h$ satisfying for all $v_r \in X_r$,

$$((U_h + w_r)_t, v_r) + b^*((U_h + w_r), (U_h + w_r), v_r) + \nu(\nabla(U_h + w_r), \nabla v_r) = 0,$$

143 and then recover the solution via $u_r(t) = U_h + w_r(t)$. Since $(U_h)_t = 0$ and $X_r \subset V_h$ implies that
144 $(\nabla U_h, \nabla v_r) = 0$, the ROM reduces to: Find $w_r(t) \in X_r \subset V_h$ satisfying for all $v_r \in X_r$,

$$((w_r)_t, v_r) + b^*((U_h + w_r), (U_h + w_r), v_r) + \nu(\nabla w_r, \nabla v_r) = 0. \tag{3.6}$$

The ROM with the Stokes extension is summarized in Algorithm 1:

Algorithm 1 ROM with the Stokes Extension

Step 1 In the offline stage, find the solution U_h of the Stokes problem (3.5).
Step 2 In the online stage, use U_h from Step 1 to construct the ROM (3.6).

145

6

146 The discrete energy balance of this ROM is revealed by choosing $v_r = w_r$, which provides

$$\frac{d}{dt}\frac{1}{2}\|w_r\|^2 + b^*((U_h + w_r), (U_h + w_r), w_r) + \nu\|\nabla w_r\|^2 = 0.$$

147 Properties of the skew-symmetric operator now provide the discrete ROM energy balance that is
148 analogous to the continuous balance (3.1):

$$\frac{d}{dt}\frac{1}{2}\|w_r\|^2 + \nu\|\nabla w_r\|^2 = -b^*(u_r, U_h, w_r). \tag{3.7}$$

149 Moreover, an analogously defined modified energy, $\tilde{E}_r(t) = \frac{1}{2}\left(\|w_r(t)\|^2 + \|U_h\|^2\right)$ has en exact bal-
150 ance analogous to the continuous case in (3.2):

$$\frac{d}{dt}\tilde{E}_r(t) + \nu\|\nabla w_r\|^2 = -b^*(u_r, U_h, w_r). \tag{3.8}$$

151 *3.2. Energy Balance for U_h the Average of Snapshots*

152 We have shown above that if U_h is the discrete Stokes extension of the boundary condition,
153 then the continuous level energy balance matches the discrete energy balance. We consider now
154 U_h to be the average of the snapshots (the most common choice), and the ROM becomes: Find
155 $w_r(t) \in X_r \subset V_h$ satisfying for all $v_r \in X_r$,

$$((w_r)_t, v_r) + b^*((U_h + w_r), (U_h + w_r), v_r) + \nu(\nabla(U_h + w_r), \nabla v_r) = 0,$$

156 and then recover the solution via $u_r(t) = U_h + w_r(t)$. Note that in this case $\nu(\nabla U_h, \nabla v_r) \neq 0$ in
157 general, since there is no reason why this U_h should be perpendicular to V_h. Now choosing $v_r = w_r$
158 yields the energy balance:

$$\frac{d}{dt}\frac{1}{2}\|w_r\|^2 + \nu\|\nabla w_r\|^2 + \nu(\nabla U_h, \nabla w_r) = -b^*(u_r, U_h, w_r). \tag{3.9}$$

159 The obvious difference between this balance and the balance (3.7) is the term $\nu(\nabla U_h, \nabla w_r)$ on the
160 left hand side of (3.9). Our issue with this discrete energy balance is that *it is not clear* that there
161 is a matching continuous level energy balance; we concede that we are not sure that one does not
162 exist, although it seems unlikely. One immediate issue for defining a continuous level balance is how
163 to define the analogous continuous level U; one possibility would be the long time average of the
164 continuous NSE, but such a U may not exist uniquely without unrealistic small data assumptions.
165 But even if it did exist uniquely, it is not clear that it would lead to an energy balance that matches
166 (3.9) due to the Reynolds stress terms present in the definition of the long time average solution.

167 Although this presents an open question regarding the validity of (3.9), it is straightforward
168 to test ROMs where U_h is defined with cases (i) and (ii), and monitor the evolution of the energy
169 with time. We do precisely this in section 5, and our tests clearly reveal that the energy for the
170 ROM defined with U_h as the discrete Stokes extension of the boundary condition matches the DNS
171 energy very well, while the ROM defined with U_h as the snapshot average has an energy that grows
172 significantly in time (see figure 4).

173 **Remark 3.1.** *The above analysis shows that using the Stokes extension of the boundary condition*
174 *leads to an accurate discrete energy balance, but using the snapshot average seemingly does not.*
175 *However, there can be other "correct" choices for U_h; steady NSE extension of the boundary condi-*
176 *tion would also lead to matching continuous and discrete energy balance. However, since the Stokes*
177 *extension is simpler, we consider only this type of extension in our numerical tests.*

4. Mass Conservation in ROMs

In this section, we consider the effect of the type of mass conservation enforcement in the snapshots (i.e. weak versus strong) on the ROM accuracy. To this end, we consider ROMs built from snapshots generated with the numerical algorithm (2.6) with two types of FEs: (i) the standard *Taylor-Hood (TH)* element, which satisfies the mass conservation weakly; and (ii) the *Scott-Vogelius (SV)* element, which satisfies the mass conservation pointwise. TH is by far more popular than SV, however recent works [28, 24] have shown that the mass conservation provided by TH elements can be quite poor, even if it is 'optimal' in the asymptotic convergence sense:

$$\|\nabla \cdot u_{TH}\|_{L^2(0,T;L^2)} \leq C\|u - u_{TH}\|_{L^2(0,T;H^1)} \leq C(h^m + \Delta t^2).$$

The problem with this estimate is that the constant C can be large, as it depends on higher order seminorms of the true solution, and furthermore, in practice h and Δt do not 'go to 0'; they have fixed positive values. It is shown in several works [28, 24] that the mass conservation error can be quite large, even $O(1)$, in seemingly converged simulations using TH elements. This is demonstrated below in section 5, where DNS using SV and TH look identical, give the same, accurate, lift and drag predictions; even the ROM bases from TH and SV are visually indistinguishable. However, the TH modes have $O(1)$ and even $O(10)$ mass conservation in the $L^2(\Omega)$ norm, whereas the SV modes have zero divergence (see figure 3).

In addition to the problem of computing solutions with large divergence error, which is a serious problem if one requires physically relevant solutions, the poor mass conservation in TH elements can also adversely affect the total velocity error. This is seen in the finite element error estimate (2.7), in that the error for the TH velocity has an additional term $\nu^{-1}\|p\|_{\infty,m}^2 h^{2m}$, whereas the SV solution's error is completely independent of pressure. As discussed in [24], in certain problems this term can be the dominant error source and cause TH solutions to be significantly worse than SV solutions (in particular, problems with large or complex pressure true solutions, such as non-isothermal flow with large Rayleigh numbers). This difference in error estimates carries over to the ROM setting as well, which we show below (the result is given and discussed in this section, but the proof is moved to the appendix).

For simplicity, in the error estimate below we consider $g = 0$, however, the results can be extended to the case $g \neq 0$ with some additional work, but without major difficulty. Thus, the ROM we consider takes the form: Find $u_r^{n+1} \in X_r$ satisfying for all $v_r \in X_r$,

$$\frac{1}{2\Delta t}\left(3u_r^{n+1} - 4u_r^n + u_r^{n-1}, v_r\right) + b^*(u_r^{n+1}, u_r^{n+1}, v_r) + \nu(\nabla u_r^{n+1}, \nabla v_r) = (f^{n+1}, v_r), \qquad (4.1)$$

for $n = 1, 2, 3, \ldots, M = T/\Delta t$, and with u_r^0 and u_r^1 being projections of the DNS solution into X_r at t^0 and t^1.

A stability estimate is immediate for (4.1).

Lemma 4.1. *The solution of the ROM (4.1) satisfies the following bound:* $\forall\, 1 \leq \widetilde{M} \leq M$,

$$\left\|u_r^{\widetilde{M}}\right\|^2 + 2\nu\Delta t \sum_{n=0}^{\widetilde{M}-1}\left\|\nabla u_r^{n+1}\right\|^2 \leq \|u_r^1\|^2 + \|2u_r^1 - u_r^0\|^2 + 2\nu^{-1}\Delta t \sum_{n=0}^{\widetilde{M}-1}\left\|f^{n+1}\right\|_{-1}^2 = C(u_r^0, u_r^1, f, \nu^{-1}).$$

$$(4.2)$$

8

212 *Proof.* The proof follows by letting $\varphi_r = u_r$ in (2.10), and using the Cauchy-Schwarz and Young
213 inequalities, as well as the algebraic identity [29, 30]

$$\frac{1}{2}(3a - 4b + c)a = \frac{1}{4}[a^2 + (2a - b)^2] - \frac{1}{4}[b^2 + (2b - c)^2] + \frac{1}{4}(a - 2b + c)^2. \qquad (4.3)$$

214 □

215 **Theorem 4.1.** *Under the usual smoothness assumptions on the continuous NSE solution, and the*
216 *usual assumptions for the ROM projection error (all specifically stated in the appendix), there exists*
217 $\Delta t^* > 0$ *such that, for all $\Delta t < \Delta t^*$, the following bound holds:*

$$\|u^M - u_r^M\|^2 + \nu \, \Delta t \sum_{n=0}^{M-1} \|\nabla(u^{n+1} - u_r^{n+1})\|^2 \qquad (4.4)$$

$$\leq \quad C \left[\frac{1}{\nu} \left(1 + \|S_r\|_2 \right) \left(h^{2m} + \Delta t^4 + \left\{ \begin{array}{ll} \nu^{-1} \|p\|_{\infty,m}^2 \, h^{2m} & TH \\ 0 & SV \end{array} \right) + \sum_{j=r+1}^{d} \lambda_j + \sum_{j=r+1}^{d} |\varphi_j|_1^2 \, \lambda_j \right],$$

218 *where C depends problem data and the true velocity solution, but not on $h, \Delta t$ or the pressure true*
219 *solution p.*

220 The key observation of the theorem is that if SV elements are used, then the error estimate is
221 independent of the pressure. If TH elements are used, then for certain problems with large and/or
222 complex pressure solutions and small viscosity, the TH error could be significantly worse.

223 In our numerical tests in the next section, we observe improved accuracy in the ROM created
224 with SV snapshots compared to the TH snapshots. In addition to giving pointwise divergence-free
225 ROM solutions, the ROM created with SV snapshots also gives better lift and drag predictions,
226 and a more stable energy prediction, especially over longer times.

227 **Remark 4.1.** *An important variant of TH-FEM that one can also consider is to use grad-div*
228 *stabilization with TH-FEM, which is known to improve mass conservation and can also decrease*
229 *overall error. Moreover, it is shown in [28] that TH with grad-div stabilization gives solutions "in*
230 *between" TH-FEMs and SV-FEMs (grad-div parameter 0 gives TH-FEM, and grad-div parameter*
231 *infinity gives SV-FEM).*

232 *Although we do not discuss results of TH-ROMs created with TH-FEM using grad-div stabi-*
233 *lization, we did perform some numerical tests using stabilization parameter 1. This did provide*
234 *TH-ROMs that were slightly better than TH-ROMs without grad-div stabilization, but since the im-*
235 *provement was not dramatic, we omitted these results and a discussion of grad-div stabilization.*
236 *There may be other problems, however, where grad-div does make a more dramatic difference in*
237 *accuracy of TH-ROMs.*

238 5. Numerical Experiments

239 We present here results of numerical experiments to illustrate the theory above. All tests will
240 be on the benchmark problem of 2D channel flow past a cylinder. This is a benchmark problem
241 from [31] that is often used for testing new methods. In all the numerical experiments, we have
242 used a Reynolds number $Re = 100$. We note, however, that we have also run tests at $Re = 200$
243 and the results were qualitatively similar to those for $Re = 100$.

9

5.1. Test problem setup

The domain is a 2.2×0.41 rectangular channel with a radius=0.05 cylinder, centered at $(0.2, 0.2)$, see Figure 1. No slip boundary conditions are prescribed for the walls and on the cylinder, and the inflow and outflow profiles are given by

$$u_1(0, y, t) = u_1(2.2, y, t) = \frac{6}{0.41^2} y(0.41 - y),$$

$$u_2(0, y, t) = u_2(2.2, y, t) = 0.$$

Imposing a parabolic profile for the outflow velocity is unphysical. We note, however, that our choice of Dirichlet boundary conditions is customary in the ROM field, since it simplifies the theoretical and numerical investigation. Furthermore, we emphasize that these outflow velocity boundary conditions do not significantly affect the upstream drag and lift coefficients and is often used [32, 33]. The kinematic viscosity is $\nu = 10^{-3}$, there is no forcing ($f = 0$), and the flow starts from rest. To compute the lift and drag, we used the following formulas:

$$c_d(t) = \frac{2}{\rho L U_{max}^2} \int_S \left(\rho \nu \frac{\partial u_{t_S}(t)}{\partial n} n_y - p(t) n_x \right) \, dS,$$

$$c_l(t) = \frac{2}{\rho L U_{max}^2} \int_S \left(\rho \nu \frac{\partial u_{t_S}(t)}{\partial n} n_x - p(t) n_y \right) \, dS,$$

where u_{t_S} is the tangential velocity, $U_{max} = 1$ is the max inlet velocity, $L = 0.1$ is the cylinder diameter, $\rho = 1$ is the density, S is the cylinder, and $n = \langle n_x, n_y \rangle$ is the outward unit normal to the domain.
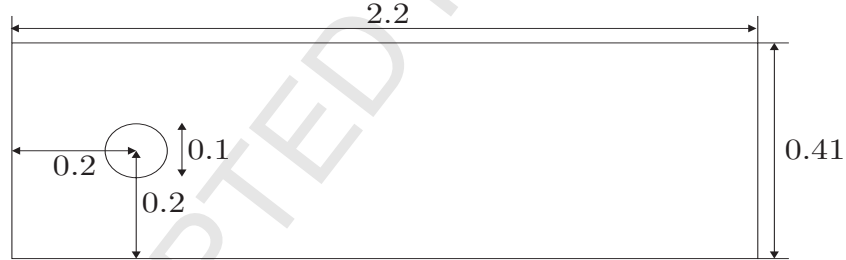

Figure 1: Shown above is the channel flow around a cylinder domain.

5.2. Snapshot Generation

The numerical scheme used to compute the snapshots is the commonly used linearized BDF2 temporal discretization, together with a finite element spatial discretization utilizing either TH or SV elements. The resulting ROMs are denoted TH-ROM and SV-ROM, respectively. Note that on time step 1, we use a backward Euler temporal discretization. The scheme for $n = 1, 2, \ldots$, is: find $(u_h^{n+1}, p_h^{n+1}) \in (X_h^g, Q_h)$ satisfying for every $(v_h, q_h) \in (X_h, Q_h)$,

$$\left(\frac{3u_h^{n+1} - 4u_h^n + u_h^{n-1}}{2\Delta t}, v_h \right) + b^* \left(u_h^{n+1}, u_h^{n+1}, v_h \right) - (p_h^{n+1}, \nabla \cdot v_h) + \nu(\nabla u_h^{n+1}, \nabla v_h) = 0,$$

$$(\nabla \cdot u_h, q_h) = 0.$$

10

260 All simulations use a time step size of $\Delta t = 0.002$, and simulations are started from rest and
261 compute to the end time $T = 17$. After an initial spin-up, the flow reaches a periodic-in-time
262 (statistically steady) state by about $T = 5$ (see plots of lift, drag, and energy evolution in figure 2).
263 Observe also from figure 2 that for the TH solution, despite its agreement in statistics with the SV
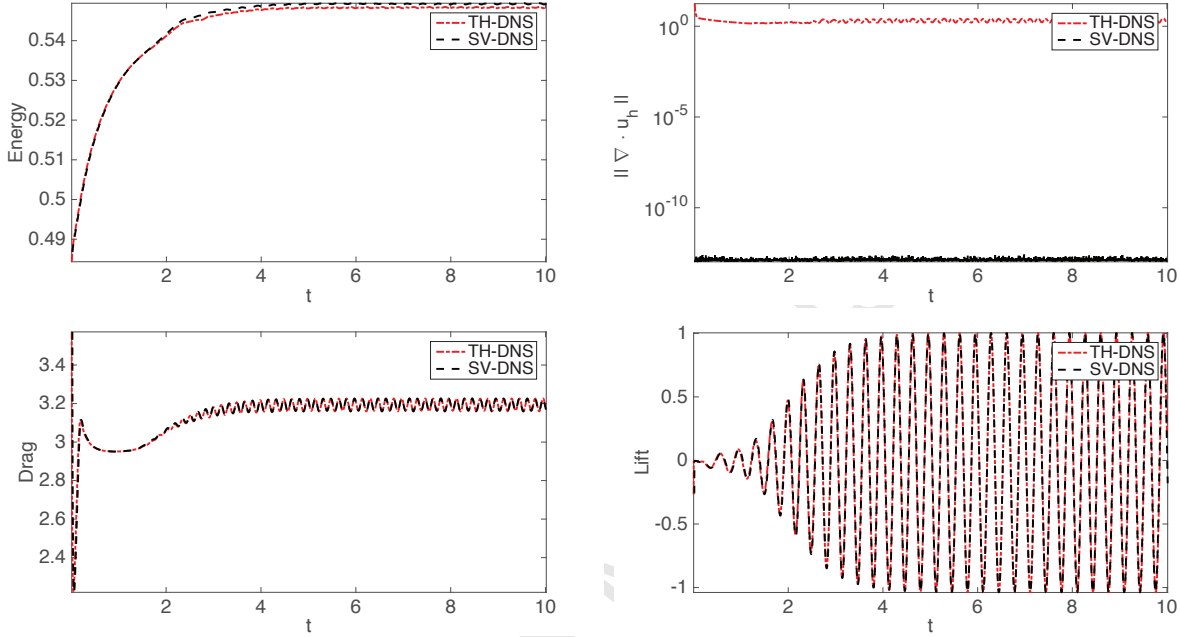264 solution, the divergence error is O(1) while the SV divergence error is around machine precision.

Figure 2: Plots of high resolution finite element (using both SV and TH elements) solutions' evolution of drag and lift coefficients, with velocity starting from rest.

265 Snapshots were taken to be the solutions at each time step from $T = 7$ to $T = 10$. We computed
266 on 4 different meshes, and with both TH and SV elements, which provided 103K, 35K, 23K, and
267 15K velocity degrees of freedom. The 103K mesh gave essentially a fully resolved solution with both
268 element choices, and the lift and drag predictions agreed well with results from fine discretizations
269 in [34, 31]:

$$c_{d,max}^{SV} = 3.2263, \ c_{l,max}^{SV} = 1.0034, \qquad c_{d,max}^{TH} = 3.2261, \ c_{l,max}^{TH} = 1.0040.$$

270 Results from the 35K meshes were only slightly less accurate, and error was more evident from the
271 23K and 15K simulations.
272 The dominant modes are created from the snapshots in the usual way. The first mode is chosen
273 to be U_h, which satisfies the boundary conditions, and we experiment below by picking U_h to be
274 both the average of the snapshots and the Stokes extension of the boundary condition. This U_h is
275 then subtracted from the snapshots, and finally an eigenvalue problem is solved to find the dominant
276 modes of these adjusted snapshots (see [34] for a more detailed description of the process). The first
277 five modes from the 103K simulations are shown in figure 3 for both TH and SV, where U_h is chosen
278 to be the average of the snapshots (the modes arising from using the Stokes extension for U_h are
279 visually indistinguishable from these modes). There is very little difference between the TH and SV
280 modes. The only difference seems to be the numerical oscillations of the SV modes at the outflow

11

281 boundary. We note, however, that these oscillations, which are likely due to the outflow boundary
282 condition implementation together with the strong implementation of the divergence constraint,
283 have a relatively low magnitude and do not have a significant effect on the ROM simulations. We
284 also emphasize that there is a huge difference in the divergences of the TH and SV modes; the TH
285 modes have $O(1)$ and even $O(10)$ divergence errors.

$\|\nabla \cdot \phi_1^{SV}\|$=1.01E-12 $\|\nabla \cdot \phi_1^{TH}\|$=7.56E-1

$\|\nabla \cdot \phi_2^{SV}\|$=4.21E-13 $\|\nabla \cdot \phi_2^{TH}\|$=4.35E-0

$\|\nabla \cdot \phi_3^{SV}\|$=4.00E-13 $\|\nabla \cdot \phi_3^{TH}\|$=7.96E-0

$\|\nabla \cdot \phi_4^{SV}\|$=3.92E-13 $\|\nabla \cdot \phi_4^{TH}\|$=1.32E+1

$\|\nabla \cdot \phi_5^{SV}\|$=3.64E-13 $\|\nabla \cdot \phi_5^{TH}\|$=1.42E+1
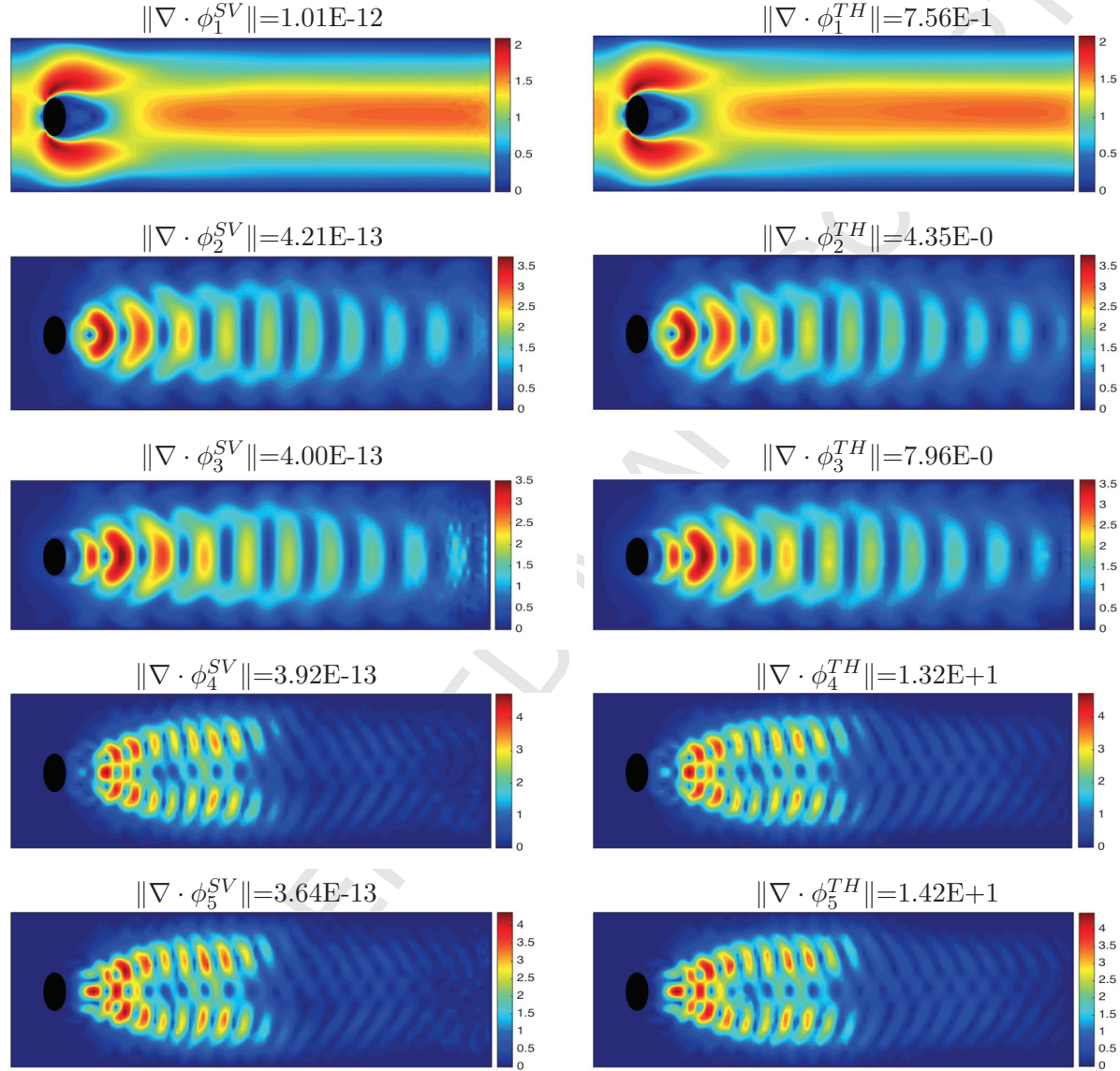
Figure 3: The first 5 dominant modes arising from the SV (left) and TH (right) snapshots. Although very similar, their differences in divergence error is dramatic.

286   With the dominant modes created, the ROM is constructed as discussed in section 2 using the
287 BDF2 temporal discretization, and at each time step takes the form: find $u_r^{n+1} = U_h + w_r^{n+1} \in X_r$
288 satisfying for all $v_r \in X_r$,

$$\frac{1}{2\Delta t}\left(3u_r^{n+1} - 4u_r^n + u_r^{n-1}, v_r\right) + b^*(u_r^{n+1}, u_r^{n+1}, v_r) + \nu(\nabla u_r^{n+1}, \nabla v_r) = 0, \qquad (5.1)$$

12

where X_r is the span of the first N modes (but not including the average U_h). In all of our tests, just as in the finite element simulations, we take $\Delta t = 0.002$; this choice creates no significant temporal error in any of our simulations (tests were done with varying Δt to verify that 0.002 is sufficiently small). For simplicity, we also use a second order extrapolation of the first term in the nonlinearity, $u_r^{k+1} \approx 2u_r^k - u_r^{k-1}$, as testing showed this approximation did not affect the error in our tests. The ROM initial conditions are the L^2 projections of the finite element solutions at $T = 6.998$ and $T = 7$ into the ROM space. The ROMs are run from this initial time (now called $t = 0$), and continued to $t = 10$. The ROMs also use $N = 8, N = 10$, and $N = 12$. Lower N values yield inaccurate results for all ROMs.

5.3. Numerical Tests of Energy Balance in ROMs: Comparison of Results for Different Choices of U_h

We now consider the effect of different choices for U_h on the accuracy in the ROMs, in particular the choices of U_h to be the average of the snapshots (the common choice in the ROM community) and U_h to be the Stokes extension of the boundary condition. We showed in section 3 that if U_h is chosen from the Stokes extension of the boundary condition, then a discrete energy balance that matches the continuous energy balance is obtained. However, if U_h is chosen to be the average of the snapshots, a matching discrete and continuous energy balance seemingly does not exist. We now test these two choices on the flow past a cylinder experiment.
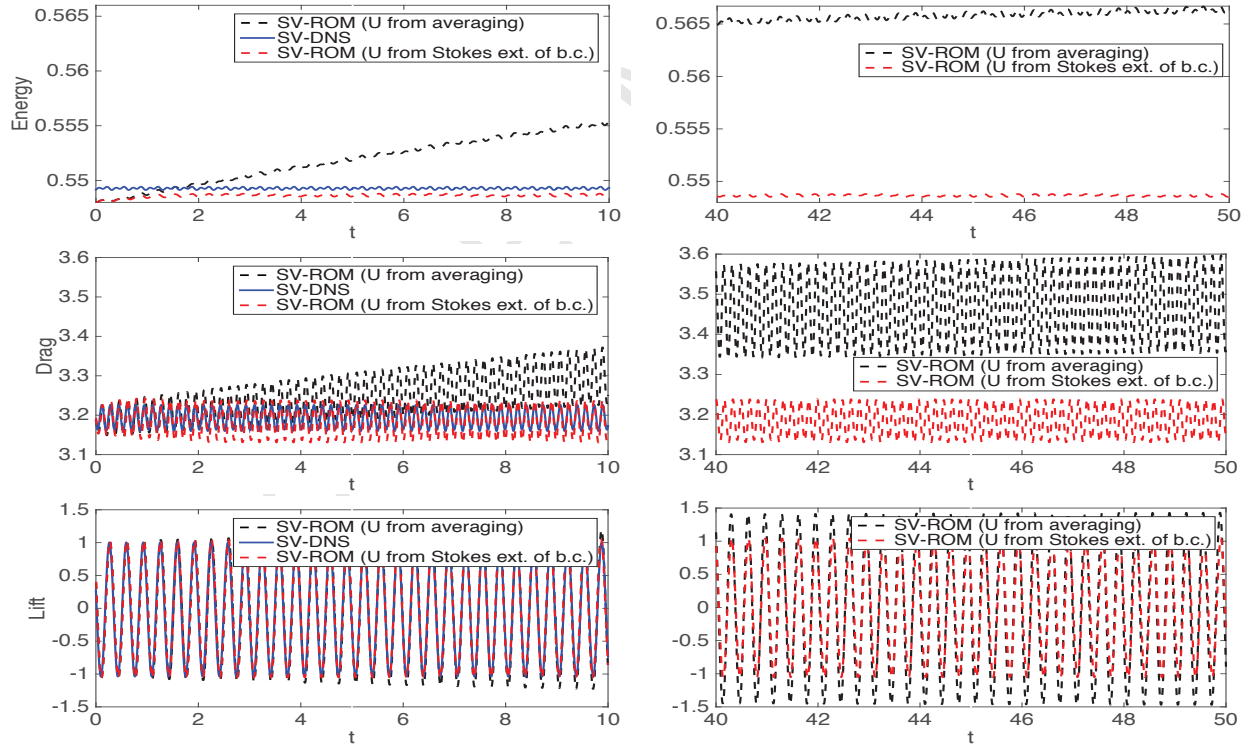

Figure 4: Plots of ROM solutions' energy, drag and lift coefficients vs. time (time from 0 to 50), using centering trajectories defined by Stokes extension and snapshot average. The ROMs were created using the 23K FEM simulations with SV elements, and used $N = 8$ modes, BDF2 time stepping, and $\Delta t = 0.002$. Also shown is the FEM energy, lift and drag using BDF2 and $\Delta t = 0.002$. The plots on the left are for [0,10], and the plots on the right are for [40,50]; note that the FEM solution is only computed up to $t=10$.

13

Using SV-ROMs created from the 23K degree of freedom simulations using these two choices of U_h, we chose $N = 8$ and ran the ROM simulations to $t = 50$. Plots of energy, lift and drag for these simulations, as well as the corresponding 103K DNS statistics, are shown in figure 4. The key observation here is from the energy evolution: we observe that the ROM that uses the Stokes extension for U_h gives a stable energy that behaves very similar to the DNS energy (although slightly smaller, which is expected in a ROM). The energy for the ROM with U_h being the snapshot average gives an energy that significantly grows with time. This energy growth is slow, and if the simulation were run to just $t = 2$, might not even be considered significant. However, by $t = 10$, the growth has created a significant increase in the ROM energy, and by $t = 50$, it is very inaccurate. The lift and drag associated with the growing energy become less accurate with time, as one would expect. Hence we conclude that the results for the Stokes extension U_h provide a significant improvement over the snapshot average, especially over longer time.

5.4. Numerical Tests of Mass Conservation in ROMs: Comparison of Results for ROMs Built with SV and TH Elements

In this section, we investigate ROM error for ROMs created with SV and TH elements on the various meshes. We have already observed in section 5.2 that the divergence error of the TH-ROM basis functions is O(1) or larger (even on a relatively fine mesh!), whereas SV-ROM basis functions have divergence error on the order of machine error. Hence if one is interested in solutions where the divergence error is small, TH-ROM is already shown to be a bad choice. Thus we consider here accuracy of the various ROMs in terms of energy, lift and drag prediction for flow past a cylinder. Additionally, we consider TH-ROMs that use skew-symmetry and that use the convective formulation (recall for SV these are equivalent). Predictions of energy, lift and drag versus time are shown in figure 5, for the DNS, SV-ROM, and the TH-ROMs with both skew-symmetric and convective forms of the nonlinearity.

Figure 5 shows the results for ROMs built from 23K and 103K velocity degrees of freedom finite element simulations, both using $N = 10$ ($N = 8$ and $N = 12$ yield the same conclusions). We observe that in all cases, the SV-ROMs give the best predictions of energy, whereas the TH-ROMs exhibit incorrect energy growth (or decay); by $t = 10$ these errors in energy accumulate to a significant amount of nonphysical energy error. The SV-ROM also gives (by far) the best predictions of lift and drag. For the ROMs built from 23K FEMs, the drag prediction by both TH-ROMs is terrible and the lift prediction by both TH-ROMs is bad, while the SV-ROM does a good job at predicting both of these quantities even up to $t = 10$. For the ROMs built from the finer mesh (103K) FEM simulations, all methods do a good job at lift prediction, but SV-ROM does a much better job than the TH-ROMs with drag prediction: TH-ROM(skew) over-predicts drag and TH-ROM(conv) under-predicts it. The over- and under-predictions correlate very closely with the respective methods' over- and under-prediction of energy.

We also provide numerical results for lift and drag, and their ranges, in table 1. The table gives results for $N = 8$ and $N = 12$, for the four different meshes, for the SV-ROMs and the TH-ROM (both with convective and skew-symmetric forms of the nonlinearity). These results give the same general results as the plots above: the SV-ROM is more accurate than the TH-ROMs, in particular on ROMs built from coarser meshes.

14

ROMs built from 23K FEM simulations
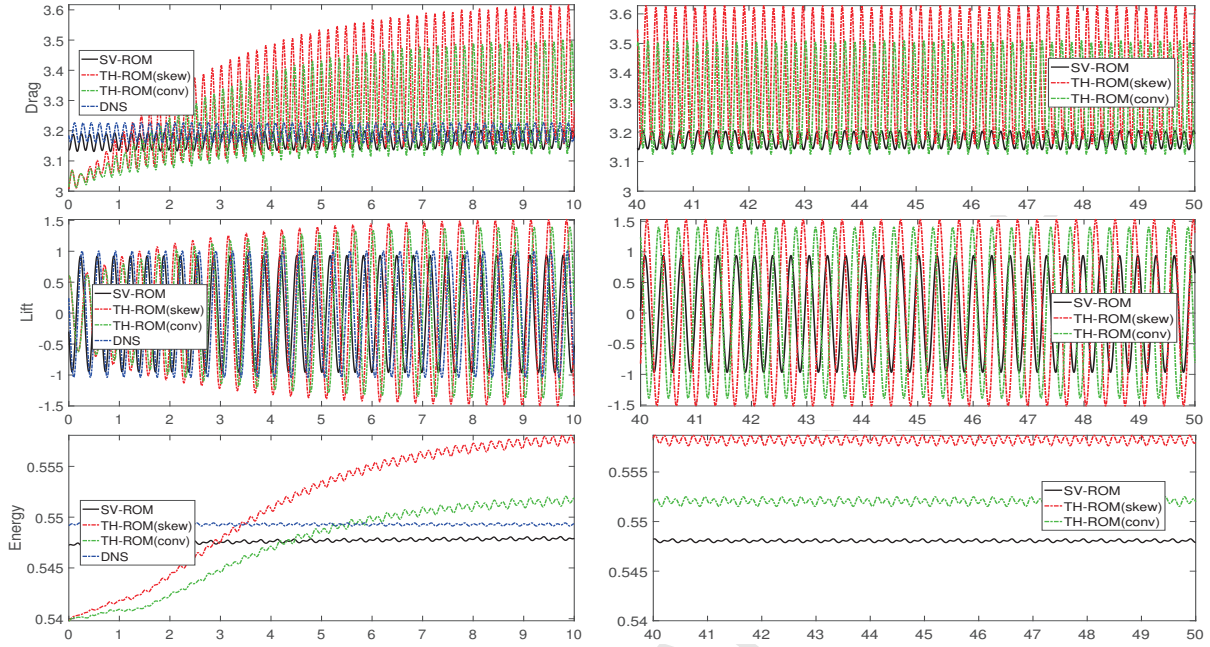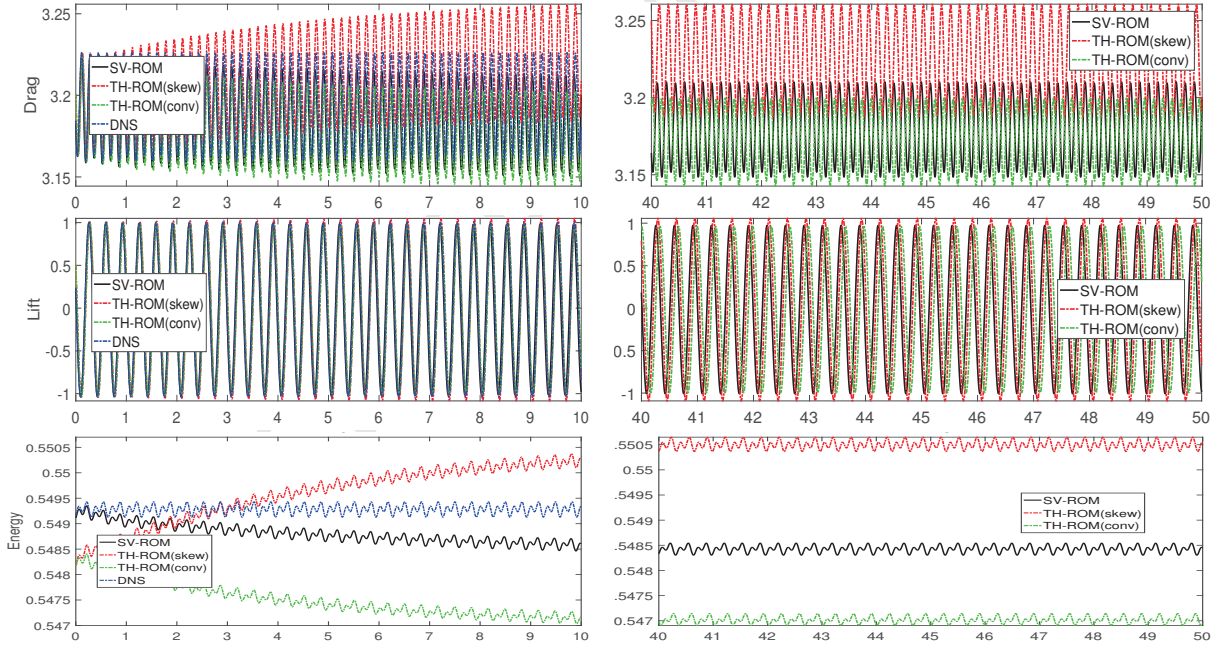

ROMs built from 103K FEM simulations

Figure 5: Plots of ROM solutions' drag, lift coefficients and energy vs. time, for flow past a cylinder with $Re = 100$, for ROMs built with 23K (top) and 103K (bottom) velocity degrees of freedom finite elements simulations.

6. Conclusions and Future Work

In this paper, we performed a theoretical and computational investigation of the conservation properties of ROMs for fluid flows modeled by the NSE. Specifically, we investigated whether

15

N	Element	FEM dof	NL form	C_d^{ave}	Error	C_d^{range}	Error	C_l^{ave}	Error	C_l^{range}	Error
	TH/SV	103K	both	3.16	-	0.07	-	-0.02	-	2.04	-
8	SV	23K	both	3.20	0.04	0.14	0.07	-0.03	0.01	2.09	0.05
8	TH	23K	skew	3.35	0.19	0.64	0.57	-0.01	0.01	3.14	1.1
8	TH	23K	conv	3.29	0.13	0.57	0.50	-0.01	0.01	2.95	0.91
8	SV	35K	both	3.24	0.08	0.20	0.13	-0.02	<0.01	2.34	0.3
8	TH	35K	skew	3.40	0.24	0.68	0.61	-0.03	0.01	3.23	1.19
8	TH	35K	conv	3.26	0.10	0.28	0.21	-0.02	<0.01	2.46	0.42
8	SV	103K	both	3.25	0.09	0.23	0.16	-0.02	<0.01	2.39	0.35
8	TH	103K	skew	3.36	0.20	0.51	0.44	-0.02	<0.01	2.97	0.93
8	TH	103K	conv	3.29	0.13	0.33	0.26	-0.02	<0.01	2.61	0.57
12	SV	23K	both	3.16	<0.01	0.06	0.01	-0.02	<0.01	1.88	0.16
12	TH	23K	skew	3.28	0.12	0.50	0.43	-0.02	<0.01	2.72	0.68
12	TH	23K	conv	3.20	0.04	0.33	0.26	-0.02	<0.01	2.38	0.34
12	SV	35K	both	3.18	0.02	0.07	< 0.01	-0.02	<0.01	2.04	<0.01
12	TH	35K	skew	3.27	0.11	0.28	0.21	-0.02	<0.01	2.56	0.52
12	TH	35K	conv	3.17	0.01	0.07	< 0.01	-0.02	<0.01	1.99	0.05
12	SV	103K	both	3.19	0.03	0.07	< 0.01	-0.02	<0.01	2.04	<0.01
12	TH	103K	skew	3.25	0.09	0.17	0.10	-0.02	<0.01	2.35	0.31
12	TH	103K	conv	3.20	0.04	0.07	< 0.01	-0.02	<0.01	2.06	0.02

Table 1: Shown above are average lift and drag coefficients, as well as the range of the lift and drag coefficients. We denote $C_d^{range} = |C_d^{max} - C_d^{min}|$ and $C_l^{range} = |C_l^{max} - C_l^{min}|$.

the standard ROMs satisfy the same (or similar) energy balance and mass conservation as those satisfied by the continuous system (i.e., the NSE). In the numerical investigation, we used the 2D flow past a circular cylinder at a Reynolds number $Re = 100$ with different mesh resolutions and ROM dimensions.

Our first contribution was the investigation of the ROM energy balance when two different types of centering trajectories were subtracted from the snapshots to tackle nonhomogeneous boundary conditions. The first centering trajectory considered was the snapshot average, which is by far the most popular choice in the ROM literature. The second centering trajectory considered was the Stokes extension; to our knowledge, this is new in the ROM setting. In section 3, we showed that the standard ROM using the Stokes extension satisfies the same energy balance as the continuous level NSE. However, the standard ROM using the snapshot average satisfies an energy balance that is different from the NSE one. The numerical investigation in section 5.3 confirmed our theoretical findings: The ROM using the Stokes extension yielded accurate values for the energy, drag, and lift evolution. However, the energy, drag, and lift of the ROM using the snapshot average displayed unphysical growth, especially over longer time intervals.

Our second contribution was the investigation of ROM mass conservation when two types of FEs were used to generate the snapshots. The first one was the standard Taylor-Hood (TH) element, which satisfies the mass conservation weakly. The second element considered was the Scott-Vogelius (SV) element, which satisfies the mass conservation pointwise. The ROMs constructed from snapshots generated with the two elements were denoted as TH-ROM and SV-ROM. In section 4 and in the appendix we proved that, just as in the FE case, the error estimates for the SV-ROM were sharper than those for the TH-ROM. Specifically, we showed that the TH-ROM error estimates had an extra term that scaled as the Reynolds number and the norm of the pressure. The numerical results in section 5.4 confirmed the theoretical findings: The SV-ROM energy, drag, and lift were accurate. The TH-ROM, on the other hand, consistently either over-predicted or under-predicted the energy, drag, and lift, especially for coarser meshes and longer time intervals.

16

377 An important future direction for this work is to improve additional physics in ROMs. In this
378 paper, we showed how to obtain accurate discrete energy balances, but there are additional physical
379 balances that ROMs typically do not account for, including momentum, angular momentum and
380 helicity. Recent work in [4] shows how to obtain correct discrete balances for these quantities in
381 finite element discretizations, and the possibility of extending these ideas to the ROM arena is
382 certainly worthy of exploration.

383 The analysis in section 3 and the supporting numerical results in section 5.3 showed that using
384 the Stokes extension of the boundary condition leads to an accurate discrete energy balance, but
385 using the snapshot average seemingly does not. However, there can be other "correct" centering
386 trajectory choices. For example, the steady NSE extension of the boundary condition would also
387 lead to matching continuous and discrete energy balance (see Remark 3.1). The theoretical and
388 numerical investigation of such centering trajectory alternatives is another interesting research
389 direction.

390 Finally, we note that although the results obtained for $Re = 200$ were qualitatively similar
391 to those for $Re = 100$, a more careful numerical investigation is needed to study whether the
392 conclusions drawn in this paper are valid for a wider range of Reynolds numbers. This represents
393 another research direction worthy of exploration.

Acknowledgments

Appendix A. Proof of Theorem 4.1

398 The purpose of the appendix is to rigorously prove Theorem 4.1. To do so, we first provide
399 some technical preliminaries, and then prove the result. Our analysis collects several results [35,
400 36, 37, 38, 39, 40, 41] in order to prove the error estimate.

401 To ensure the uniqueness of the NSE solution and ensure that the finite element error estimate
402 (2.7) holds (the finite element error estimate is used in the ROM error estimate), we make the
403 following common regularity assumptions on the data and true solution: $f \in L^2(0,T;L^2(\Omega)), u^0 \in$
404 $V, u \in L^\infty(0,T;H^{k+1}(\Omega)), u_t \in L^\infty(0,T;L^2(\Omega)), u_{tt} \in L^\infty(0,T;L^2(\Omega))$, and $p \in L^\infty(0,T;Q \cap$
405 $H^k(\Omega))$ (for TH elements only).

406 Let $S_r \in \mathbb{R}^{r \times r}$ with $(S_r)_{ij} = (\nabla \varphi_j, \nabla \varphi_i)_{L^2}$ be the ROM stiffness matrix and let $\|\cdot\|_2$ denote the
407 matrix 2-norm.

Lemma Appendix A.1 (ROM Inverse Estimates)**.** *For all $v_r \in X_r$, the following ROM inverse
estimate holds [38]:*

$$\|\nabla v_r\| \leq \sqrt{\|S_r\|_2} \|v_r\|. \tag{A.1}$$

410

Definition Appendix A.1 (ROM L^2 Projection)**.** *Let $P_r : L^2 \to X_r$ such that, $\forall v \in L^2, P_r(v)$ is
the unique element of X_r such that*

$$(P_r(v), v_r) = (v, v_r) \quad \forall v_r \in X_r. \tag{A.2}$$

17

413   We assume the following error estimate, which is similar to the assumptions made in [36, 42, 43].

414 **Assumption Appendix A.1.** *The L^2 ROM projection of u^n, $P_r(u^n)$, satisfies the following error*
415 *estimates:*

$$\max_n \|u^n - P_r(u^n)\|^2 \leq C \left(h^{2m} + \Delta t^4 + \left\{ \begin{array}{ll} \nu^{-1} \|p\|_{\infty,m}^2 \, h^{2m} & \text{if } TH \\ 0 & \text{if } SV \end{array} \right. \right) + \sum_{j=r+1}^{d} \lambda_j \quad \text{(A.3)}$$

$$\max_n \|\nabla (u^n - P_r(u^n))\|^2 \leq \frac{1}{\nu} \left(1 + \|S_r\|_2 \right) C \left(h^{2m} + \Delta t^4 + \left\{ \begin{array}{ll} \nu^{-1} \|p\|_{\infty,m}^2 \, h^{2m} & \text{if } TH \\ 0 & \text{if } SV \end{array} \right. \right)$$

$$+ \sum_{j=r+1}^{d} |\varphi_j|_1^2 \, \lambda_j. \quad \text{(A.4)}$$

416

417   The assumption above is for the maximum errors in time, however it is known from Lemma 3.3
418 in [42] that this result does hold for the average over $1 \leq k \leq M$. Hence the assumption boils down
419 to whether most snapshots have ROM projection errors that are of the same order of magnitude.
420 If there were a case where, for example, most of the snapshots were (up to machine precision) in
421 the span of the ROM basis, then the max error assumption would only hold up to the constant C
422 now depending on Δt^{-1} (see Remark 3.2 in [42]).

423   We can now prove the theorem, under the assumptions above for regularity and the ROM
424 projection error.

425 *Proof.* At time t^{n+1}, testing the NSE with $v_r = \varphi_r$ produces

$$(u_t^{n+1}, \varphi_r) + b^*(u^{n+1}, u^{n+1}, \varphi_r) + \nu(\nabla u^{n+1}, \nabla \varphi_r) - (p, \nabla \cdot \varphi_r) = (f^{n+1}, \varphi_r). \quad \text{(A.5)}$$

426 Subtracting (4.1) from (A.5), we obtain

$$\left(u_t^{n+1} - \frac{3u_r^{n+1} - 4u_r^n + u_r^{n-1}}{2\Delta t}, \varphi_r \right) + b^*(u^{n+1}, u^{n+1}, \varphi_r) - b^*(u_r^{n+1}, u_r^{n+1}, \varphi_r)$$

$$+ \nu(\nabla u^{n+1} - \nabla u_r^{n+1}, \nabla \varphi_r) - (p, \nabla \cdot \varphi_r) = 0. \quad \text{(A.6)}$$

427 Adding and subtracting $(\frac{3u^{n+1} - 4u^n - u^{n-1}}{2\Delta t}, \varphi_r)$, we have

$$\left(u_t^{n+1} - \frac{3u^{n+1} - 4u^n + \mathbf{u}^{n-1}}{2\Delta t}, \varphi_r \right) + \left(\frac{3u^{n+1} - 4u^n + \mathbf{u}^{n-1}}{2\Delta t} - \frac{3u_r^{n+1} - 4u_r^n + u_r^{n-1}}{2\Delta t}, \varphi_r \right)$$

$$+ b^*(u^{n+1}, u^{n+1}, v) - b^*(u_r^{n+1}, u_r^{n+1}, \varphi_r) + \nu(\nabla u^{n+1} - \nabla u_r^{n+1}, \nabla \varphi_r) = (p, \nabla \cdot \varphi_r). \quad \text{(A.7)}$$

We decompose the error as follows:

$$u^{n+1} - u_r^{n+1} = (u^{n+1} - w_r^{n+1}) - (u_r^{n+1} - w_r^{n+1}) = \eta^{n+1} - \phi_r^{n+1},$$

428 where $w_r^{n+1} = P_r(u^{n+1})$ is the L^2 projection of u^{n+1}:

$$(u^{n+1} - w_r^{n+1}, \varphi_r) = 0, \ \forall \varphi_r \in X_r. \quad \text{(A.8)}$$

18

429 Choosing $\varphi_r = \phi_r^{n+1}$ and letting $r^{n+1} = u_t^{n+1} - \frac{3u^{n+1}-4u^n+u^{n-1}}{2\Delta t}$, (A.7) becomes

$$\frac{1}{2\Delta t}\left(3\eta^{n+1} - 3\phi_r^{n+1} - 4(\eta^n - \phi_r^n) + \eta^{n-1} - \phi_r^{n-1}, \phi_r^{n+1}\right) - \nu(\nabla\phi_r^{n+1}, \nabla\phi_r^{n+1}) + \nu(\nabla\eta^{n+1}, \nabla\phi_r^{n+1})$$
$$+b^*(u^{n+1}, u^{n+1}, \phi_r^{n+1}) - b^*(u_r^{n+1}, u_r^{n+1}, \phi_r^{n+1}) + (r^{n+1}, \phi_r^{n+1}) = (p, \nabla \cdot \phi_r^{n+1}). \tag{A.9}$$

430 Since $\phi_r^i \in X_r, i = n - 1, n, n + 1$, (A.8) implies that $(\eta, \phi_r^i) = 0$. Thus, (A.9) becomes

$$\frac{1}{2\Delta t}\left(3\phi_r^{n+1} - 4\phi_r^n + \phi_r^{n-1}, \phi_r^{n+1}\right) + \nu(\nabla\phi_r^{n+1}, \nabla\phi_r^{n+1}) = (r^{n+1}, \phi_r^{n+1}) + \nu(\nabla\eta^{n+1}, \nabla\phi_r^{n+1})$$
$$+b^*(u^{n+1}, u^{n+1}, \phi_r^{n+1}) - b^*(u_r^{n+1}, u_r^{n+1}, \phi_r^{n+1}) - (p, \nabla \cdot \phi_r^{n+1}). \tag{A.10}$$

431 The nonlinearity contribution to (A.10) can be decomposed as follows:

$$b^*(u^{n+1}, u^{n+1}, \phi_r^{n+1}) - b^*(u_r^{n+1}, u_r^{n+1}, \phi_r^{n+1})$$
$$= b^*(u^{n+1} - u_r^{n+1}, u^{n+1}, \phi_r^{n+1}) + b^*(u_r^{n+1}, u^{n+1} - u_r^{n+1}, \phi_r^{n+1})$$
$$= b^*(\eta^{n+1}, u^{n+1}, \phi_r^{n+1}) - b^*(\phi_r^{n+1}, u^{n+1}, \phi_r^{n+1}) + b^*(u_r^{n+1}, \eta^{n+1}, \phi_r^{n+1}), \tag{A.11}$$

432 where we used the fact that $b^*(u_r^{n+1}, \phi_r^{n+1}, \phi_r^{n+1}) = 0$. Using Hölder, Cauchy-Schwarz and Young
433 inequalities, along with standard Sobolev inequalities, we estimate the terms on the RHS of (A.10)
434 as follows:

$$b^*(u_r^{n+1}, \eta^{n+1}, \phi_r^{n+1}) \leq C\|u_r^{n+1}\|^{1/2}\|\nabla u_r^{n+1}\|^{1/2}\|\nabla\eta^{n+1}\|\|\nabla\phi_r^{n+1}\|$$
$$\leq \frac{1}{4c_1}C^2\|u_r^{n+1}\|\|\nabla u_r^{n+1}\|\|\nabla\eta^{n+1}\|^2 + c_1\|\nabla\phi_r^{n+1}\|^2 \tag{A.12}$$

$$b^*(\eta^{n+1}, u^{n+1}, \phi_r^{n+1}) \leq C\|\nabla\eta^{n+1}\|\|\nabla u^{n+1}\|\|\nabla\phi_r^{n+1}\|$$
$$\leq \frac{1}{4c_2}C^2\|\nabla u^{n+1}\|^2\|\nabla\eta^{n+1}\|^2 + c_2\|\nabla\phi_r^{n+1}\|^2 \tag{A.13}$$

$$b^*(\phi_r^{n+1}, u^{n+1}, \phi_r^{n+1}) \leq C\|\phi_r^{n+1}\|^{1/2}\|\nabla\phi_r^{n+1}\|^{1/2}\|\nabla u^{n+1}\|\|\nabla\phi_r^{n+1}\|$$
$$= C\|\phi_r^{n+1}\|^{1/2}\|\nabla\phi_r^{n+1}\|^{3/2}\|\nabla u^{n+1}\|$$
$$\leq \frac{3^3 C^4}{4^4 c_3^3}\|\nabla u^{n+1}\|^4\|\phi_r^{n+1}\|^2 + c_3\|\nabla\phi_r^{n+1}\|^2. \tag{A.14}$$

435 The pressure term $(p, \nabla \cdot \phi_r^{n+1})$ needs to be treated carefully. If the SV element is used, then this
436 term simply vanishes. If the TH element is used, then this term does not vanish, and we proceed
437 with the TH case, but will track the resulting terms in order to be more precise with the SV result.
438 Since $\phi_r^{n+1} \in X_r \subset V^h$, the pressure term in (A.10) can be written as

$$-(p, \nabla \cdot \phi_r^{n+1}) = -(p - q_h, \nabla \cdot \phi_r^{n+1}) \leq \frac{C^*}{4 c_4}\|p - q_h\|^2 + C^* c_4\|\nabla\phi_r^{n+1}\|^2. \tag{A.15}$$

439 For the remaining terms on the RHS, we use standard estimates to obtain

$$(r^{n+1}, \phi_r^{n+1}) \leq \|r^{n+1}\|_{-1}\|\nabla\phi_r^{n+1}\| \leq c_5\|\nabla\phi_r^{n+1}\|^2 + \frac{1}{4c_5}\|r^n\|_{-1}^2. \tag{A.16}$$

$$\nu(\nabla\eta^{n+1}, \nabla\phi_r^{n+1}) \leq \nu\|\nabla\eta^{n+1}\|\|\nabla\phi_r^{n+1}\| \leq c_6\nu\|\nabla\phi_r^{n+1}\|^2 + \frac{\nu}{4c_6}\|\nabla\eta^{n+1}\|^2. \tag{A.17}$$

19

440 Applying the algebraic identity (4.3), the left hand side of (A.10) can be written as

$$
\begin{aligned}
LHS &= \frac{1}{4\Delta t}(\|\phi_r^{n+1}\|^2 + \|2\phi_r^{n+1} - \phi_r^n\|^2) - \frac{1}{4\Delta t}(\|\phi_r^n\|^2 + \|2\phi_r^n - \phi_r^{n-1}\|^2) \\
&+ \frac{1}{4\Delta t}\|(\phi_r^{n+1} - 2\phi_r^n + \phi_r^{n-1})\|^2 + \nu\|\nabla\phi_r^{n+1}\|^2.
\end{aligned} \tag{A.18}
$$

441 Substituting (A.12)–(A.18) into (A.10), we get

$$
\begin{aligned}
&\frac{1}{4\Delta t}(\|\phi_r^{n+1}\|^2 + \|2\phi_r^{n+1} - \phi_r^n\|^2) - \frac{1}{4\Delta t}(\|\phi_r^n\|^2 + \|2\phi_r^n - \phi_r^{n-1}\|^2) + \frac{1}{4\Delta t}\|\phi_r^{n+1} - 2\phi_r^n + \phi_r^{n-1}\|^2 \\
&+ (\nu - c_1 - c_2 - c_3 - C^* c_4 - c_5 - c_6\nu)\,\|\nabla\phi_r^{n+1}\|^2 \\
&\leq \frac{1}{4c_1}C^2\|u_r^{n+1}\|\|\nabla u_r^{n+1}\|\|\nabla\eta^{n+1}\|^2 + \frac{1}{4c_2}C^2\|\nabla u^{n+1}\|^2\|\nabla\eta^{n+1}\|^2 + \frac{3^3 C^4}{4^4 c_3^3}\|\nabla u^{n+1}\|^4\|\phi_r^{n+1}\|^2 \\
&+ \frac{C^*}{4\,c_4}\|p - q_h\|^2 + \frac{1}{4c_5}\|r^n\|_{-1}^2 + \frac{\nu}{4c_6}\|\nabla\eta^{n+1}\|^2.
\end{aligned} \tag{A.19}
$$

442 The error bound (4.4) now follows by summing (A.19) (with appropriately chosen constants), using
443 the assumptions made in the theorem, the stability estimate (4.2), a discrete Gronwall lemma (see
444 Lemma 27 in [44]), and the triangle inequality.

445 □

446 References

447 [1] T. Lassila, A. Manzoni, A. Quarteroni, G. Rozza, Model Order Reduction in Fluid Dynamics:
448 Challenges and Perspectives, Springer International Publishing, Cham, pp. 235–273.

449 [2] R. Abramov, A. Majda, Discrete approximations with additional conserved quantities: deter-
450 ministic and statistical behavior, Methods Appl. Anal. 10 (2003) 151–190.

451 [3] A. Arakawa, Computational design for long-term numerical integration of the equations of fluid
452 motion: Two dimensional incompressible flow, Part I, J. Comput. Phys. 1 (1966) 119–143.

453 [4] S. Charnyi, T. Heister, M. Olshanskii, L. Rebholz, On conservation laws of Navier-Stokes
454 Galerkin discretizations, Journal of Computational Physics 337 (2017) 289–308.

455 [5] G. Fix, Finite element models for ocean circulation problems, SIAM Journal on Applied
456 Mathematics 29 (1975) 371–387.

457 [6] J.-G. Liu, W. Wang, Energy and helicity preserving schemes for hydro and magnetohydro-
458 dynamics flows with symmetry, J. Comput. Phys. 200 (2004) 8–33.

459 [7] C. Sorgentone, S. L. Cognata, J. Nordstrom, A new high order energy and enstrophy conserving
460 Arakawa-like Jacobian differential operator, Journal of Computational Physics 301 (2015) 167–
461 177.

462 [8] R. Salmon, L. Talley, Generalizations of Arakawa's Jacobian, J. Comput. Phys. 83 (1989)
463 247–259.

20

[9] M. J. Balajewicz, E. H. Dowell, B. R. Noack, Low-dimensional modelling of high-Reynolds-number shear flows incorporating constraints from the Navier–Stokes equation, J. Fluid Mech. 729 (2013) 285–308.

[10] M. J. Balajewicz, I. Tezaur, E. H. Dowell, Minimal subspace rotation on the Stiefel manifold for stabilization and enhancement of projection-based reduced order models for the compressible Navier–Stokes equations, J. Comput. Phys. 321 (2016) 224–241.

[11] M. F. Barone, I. Kalashnikova, D. J. Segalman, H. K. Thornquist, Stable Galerkin reduced order models for linearized compressible flow, J. Comput. Phys. 228 (2009) 1932–1946.

[12] K. Carlberg, R. Tuminaro, P. Boggs, Preserving Lagrangian structure in nonlinear model reduction with application to structural dynamics, SIAM J. Sci. Comput. 37 (2015) B153–B184.

[13] S. Chaturantabut, C. Beattie, S. Gugercin, Structure-preserving model reduction for nonlinear port-Hamiltonian systems, SIAM J. Sci. Comput. 38 (2016) B837–B865.

[14] Y. Gong, Q. Wang, Z. Wang, Structure-preserving Galerkin POD reduced-order modeling of Hamiltonian systems, Comput. Methods Appl. Mech. Engrg. 315 (2017) 780–798.

[15] I. Kalashnikova, M. F. Barone, On the stability and convergence of a Galerkin reduced order model (ROM) of compressible flow with solid wall and far-field boundary treatment, Int. J. Num. Meth. Eng. 83 (2010) 1345–1375.

[16] L. Peng, K. Mohseni, Symplectic model reduction of Hamiltonian systems, SIAM J. Sci. Comput. 38 (2016) A1–A27.

[17] C. Farhat, P. Avery, T. Chapman, J. Cortial, Dimensional reduction of nonlinear finite element dynamic models with finite rotations and energy-based mesh sampling and weighting for computational efficiency, Int. J. Num. Meth. Eng. 98 (2014) 625–662.

[18] I. Kalashnikova, S. Arunajatesan, M. F. Barone, B. G. van Bloemen Waanders, J. A. Fike, Reduced order modeling for prediction and control of large-scale systems, Sandia National Laboratories Report, SAND (2014).

[19] J.-C. Loiseau, S. L. Brunton, Constrained sparse Galerkin regression, Available as arXiv preprint at http://arxiv.org/abs/1611.03271 (2016).

[20] T. Heister, L. Rebholz, M. Xiao, Flux-preserving enforcement of inhomogeneous Dirichlet boundary conditions for strongly divergence-free mixed finite element methods for flow problems, Journal of Mathematical Analysis and Applications 438 (2016) 507–513.

[21] S. Brenner, L. R. Scott, The Mathematical Theory of Finite Element Methods, volume 15 of *Texts in Applied Mathematics*, Springer Science+Business Media, LLC, 2008.

[22] D. Arnold, J. Qin, Quadratic velocity/linear pressure Stokes elements, in: R. Vichnevetsky, D. Knight, G. Richter (Eds.), Advances in Computer Methods for Partial Differential Equations VII, IMACS, pp. 28–34.

[23] S. Zhang, A new family of stable mixed finite elements for the 3d Stokes equations, Mathematics of Computation 74 (2005) 543–554.

[24] V. John, A. Linke, C. Merdon, M. Neilan, L. G. Rebholz, On the divergence constraint in mixed finite element methods for incompressible flows, SIAM Rev. (2016).

[25] W. Layton, C. C. Manica, M. Neda, L. G. Rebholz, Numerical analysis and computational testing of a high accuracy Leray-deconvolution model of turbulence, Num. Meth. P.D.E.s 24 (2008) 555–582.

[26] P. Holmes, J. L. Lumley, G. Berkooz, Turbulence, Coherent Structures, Dynamical Systems and Symmetry, Cambridge, 1996.

[27] B. R. Noack, M. Morzynski, G. Tadmor, Reduced-Order Modelling for Flow Control, volume 528, Springer Verlag, 2011.

[28] M. Case, V. Ervin, A. Linke, L. Rebholz, A connection between Scott-Vogelius elements and grad-div stabilization, SIAM Journal on Numerical Analysis 49 (2011) 1461–1481.

[29] K. J. Galvin, L. G. Rebholz, C. Trenchea, Efficient, unconditionally stable, and optimally accurate FE algorithms for approximate deconvolution models, SIAM J. Numer. Anal. 52 (2014) 678–707.

[30] W. Layton, N. Mays, M. Neda, C. Trenchea, Numerical analysis of modular regularization methods for the BDF2 time discretization of the Navier-Stokes equations, ESAIM: Math. Model. Numer. Anal. 48 (2014) 765–793.

[31] M. Schäfer, S. Turek, The benchmark problem 'flow around a cylinder' flow simulation with high performance computers II, in E.H. Hirschel (Ed.), Notes on Numerical Fluid Mechanics 52, Braunschweig, Vieweg (1996) 547–566.

[32] V. John, Reference values for drag and lift of a two dimensional time-dependent flow around a cylinder, Int. J. Num. Meth. Fluids 44 (2004) 777–788.

[33] L. Rebholz, M. Xiao, Improved accuracy in algebraic splitting methods for Navier-Stokes equations, SIAM J. Sci. Comput. (2017). To appear.

[34] A. Caiazzo, T. Iliescu, V. John, S. Schyschlowa, A numerical investigation of velocity-pressure reduced order models for incompressible flows, J. Comput. Phys. 259 (2014) 598–616.

[35] D. Chapelle, A. Gariah, J. Sainte-Marie, Galerkin approximation with proper orthogonal decomposition: new error estimates and illustrative examples, ESAIM: Math. Model. Numer. Anal. 46 (2012) 731–757.

[36] T. Iliescu, Z. Wang, Are the snapshot difference quotients needed in the proper orthogonal decomposition?, SIAM J. Sci. Comput. 36 (2014) A1221–A1250.

[37] T. Kostova, G. Oxberry, K. Chand, W. Arrighi, Error bounds and analysis of proper orthogonal decomposition model reduction methods using snapshots from the solution and the time derivatives, arXiv preprint, http://arxiv.org/abs/1501.02004 (2015).

[38] K. Kunisch, S. Volkwein, Galerkin proper orthogonal decomposition methods for parabolic problems, Numer. Math. 90 (2001) 117–148.

[39] K. Kunisch, S. Volkwein, Galerkin proper orthogonal decomposition methods for a general equation in fluid dynamics, SIAM J. Numer. Anal. 40 (2002) 492–515 (electronic).

[40] Z. Luo, J. Chen, I. M. Navon, X. Yang, Mixed finite element formulation and error estimates based on proper orthogonal decomposition for the nonstationary Navier-Stokes equations, SIAM J. Numer. Anal. 47 (2008) 1–19.

[41] J. R. Singler, New POD error expressions, error bounds, and asymptotic results for reduced order models of parabolic PDEs, SIAM J. Numer. Anal. 52 (2014) 852–876.

[42] T. Iliescu, Z. Wang, Variational multiscale proper orthogonal decomposition: Navier-Stokes equations, Num. Meth. P.D.E.s 30 (2014) 641–663.

[43] X. Xie, D. Wells, Z. Wang, T. Iliescu, Numerical analysis of the Leray reduced order model, arXiv preprint, http://arxiv.org/abs/1702.05216 (2017).

[44] W. J. Layton, Introduction to the numerical analysis of incompressible viscous flows, volume 6, Society for Industrial and Applied Mathematics (SIAM), 2008.